Flexible and Stretchable Self-Powered Multi-Sensors Based on the N-Type Thermoelectric Response of Polyurethane/$Na_x(Ni\text{-}ett)_n$ Composites

*Kening Wan, Prospero Taroni Junior, Zilu Liu, Yi Liu, Ying Tu, Giovanni Santagiuliana, I-Chuan Hsia, Han Zhang, Oliver Fenwick, Steffi Krause, Mark Baxendale, Bob C. Schroeder, Emiliano Bilotti**

Miss K. Wan, Mr. P.T. Junior, Dr. Y. Liu, Dr. Y. Tu, Dr. G. Santagiuliana, Miss I Hsia, Dr. H. Zhang, Dr. O. Fenwick, Dr. S. Krause, Dr. E. Bilotti, School of Engineering and Materials Science, Queen Mary University of London, Mile End Road, London E1 4NS, UK
E-mail: e.bilotti@qmul.ac.uk

Miss Z. Liu, Dr. B. C. Schroeder, Department of Chemistry, University College London, 20 Gordon Street, London, WC1H 0AJ, UK

Dr. M. Baxendale, School of Physics and Astronomy, Queen Mary University of London, Mile End Road, London E1 4NS, UK

Dr. G. Santagiuliana, Dr. Han Zhang, Dr. E. Bilotti, Nanoforce Technology Ltd., Joseph Priestley Building, Queen Mary University of London, Mile End Road, E1 4NS, UK

Keywords: flexible stretchable device, self-powered, sensors, organics thermoelectricity, origami

Abstract

Flexible and stretchable electronic devices have a broad range of potential uses, from biomedical, soft robotics, health-monitoring to internet-of-things. Unfortunately, finding a robust and reliable power source remains challenging, particularly in off-the-grid and maintenance-free applications. A sought-after technological feature to overcome this challenge would be the development of autonomous, self-powered devices. Herein, a potential solution is reported exploiting a promising n-type thermoelectric (TE) compound, poly nickel-ethenetetrathiolates ($Na_x(Ni\text{-}ett)_n$). Highly stretchable n-type composite films are obtained by combining $Na_x(Ni\text{-}ett)_n$ with a commercial polyurethane (Lycra®). As high as 50 wt.% Na_x(Ni-

ett)$_n$ content composite film can withstand deformations of ~ 500% and show conductivities of ~10^{-2} S cm^{-1} and Seebeck coefficients of ~ -40 μV K^{-1}. These novel materials can be easily synthesized in large scale with continuous processes. When subjected to a small temperature difference (< 20 ºC), the films generate sufficient thermopower to be used for sensing strain (*Gauge Factor* ~ 20) and visible light (*Sensitivity Factor* ~ 36% (kW m^{-2})$^{-1}$), independently of humidity (*Sensitivity Factor* ~ 0.1 (%RH)$^{-1}$). As proof-of-concept, a wearable self-powered sensor is demonstrated by using n-type Na$_x$(Ni-ett)$_n$/Lycra® and p-type PEDOT:PSS/Lycra® elements, connected in series by hot pressing, without employing any metal connections, hence preserving good mechanical ductility and ease of processing.

1. Introduction

With the rapid improvement of our living standard, the fast-developing fields of wearable devices and soft robotics have attracted considerable attention. Smart electronic devices are in high demand, especially when characterized by flexibility, extensibility, durability and low costs. Examples of such devices include health monitoring devices[1], soft robotics [2], functional artificial skin[3], etc. Although the technology has greatly improved since the first modern applications over a century ago, most sensors are still powered by batteries, limiting their reliability and sustainability. In cases like continuous monitoring, off-the-grid and maintenance-free applications, self-powered sensors would be extremely desirable.

Towards this aim, several energy harvesting strategies have been explored, based on triboelectricity,[4] piezoelectricity,[5] pyroelectricity,[6] and others.[7] Among these, thermoelectricity is recognised as a very reliable and durable potential energy harvesting phenomenon for self-powered sensors,[8] exploiting temperature gradients found ubiquitously. Since its discovery in the early 1800s, the thermoelectric (TE) effect has been used only in niche applications due to the relative low efficiencies,[9] high processing costs, toxicity and rarity of

some of the elements (e.g. tellurium, bismuth, antimony) currently used in the manufacture of commercial devices. Nevertheless, there has been a recent renewed interest in TE technology due both to the discovery of new materials and to new applications, in conjunction with solar cells,[10] supercapacitors[11] and gating transistors[12].

Organic thermoelectrics (OTE) are new materials of great interest, owing to their lower toxicity, abundance of constitutive elements, and ease in processing by various casting techniques. Very recently, OTE based self-powered sensors have been reported. A foam coated by poly(3,4-ethylenedioxythiophene) polystyrene sulfonate (PEDOT:PSS) has been demonstrated to sense both pressure and temperature.[13] A self-powered vapour sensor, based on CNTs, has also been reported.[14] More recently, our group has developed new stretchable and tough composites made of a commercial polyurethane (PU) and PEDOT:PSS, which could autonomously sense strain. [15]

As the examples above indicate, most of the OTE materials studied so far are p-type. In order to generate higher power outputs, it is essential to have an n-type OTE counterpart, so that series connected p-n junctions can be designed. Recently, an organometallic coordination polymer, $Na_x(Ni\text{-}ett)_n$, has been reported to possess excellent TE properties, including Seebeck coefficient of -80 μV K^{-1} and an electrical conductivity of ~ 42 S cm^{-1}, combined which a relatively good air-stability and simple synthesis.[16] More recently, values of room temperature Seebeck coefficient of -128 μV K^{-1} and ZT ~ 0.3 have recently been reported for Poly(Ni-ett) prepared by electrochemical deposition.[17] But a number of challenges still restrict its commercial exploitation, including low toughness and tear resistance, in addition to poor solubility and processability. Another important aspect relates to the manufacture of TE devices. The typical TE device architecture is the in-plane π-shape [18], obtained by an assembly process of p- and n-type legs, connected in series by, typically, metal contacts. This assembly process

is time consuming and hardly scalable and the resulting structure, with metal contacts, rigid and brittle.

Herein, we present a highly stretchable n-type material based on composites of PU (Lycra®) and one of the most promising n-type OTE compound ever reported: poly sodium nickel-ethenetetrathiolates ($Na_x(Ni\text{-}ett)_n$)[16, 19] [17] to overcome all these limitations. For instance, a 50/50 composite has a high elongation to break (more than 5 times its initial length) combined with a relatively high absolute Seebeck coefficient (-40 μV K^{-1}). The composites are able to harvest sufficient power, even from small temperature differences (< 20 ºC), to autonomously sense a number of stimuli, such as strain, visible light and temperature. Moreover, by exploiting the enhanced processability of TE polymer compounds, we propose new manufacturing strategies and designs to overcome the shortfalls. The composites could simply be joined by hot pressing into a series-connected multi-leg TE flexible and stretchable devices. As an example, origami-inspired TE devices with different configurations are presented.

2. Results and Discussion

2.1. Mechanical properties and morphology

Pure $Na_x(Ni\text{-}ett)_n$ (**Figure 1**c), synthesized according to a similar procedure described by Menon *et al.* ,[19] does not dissolve in common solvents and does not form coherent films (**Figure 1**d and **Figure S1**). However, Lycra®, a commercial synthetic fibre commonly used for elastic skin-tight garments and sports attires, could be used as an elastomeric matrix for coherent, flexible and stretchable films containing $Na_x(Ni\text{-}ett)_n$. Thus, a series of $Na_x(Ni\text{-}ett)_n$ / Lycra® self-standing composite films (called "NL films" from here on), with $Na_x(Ni\text{-}ett)_n$ contents ranging from 10 to 70 wt.%, has been prepared by solution mixing and drop-casting, as described in the Experimental Methods (Section 4).

A systematic study of the NL film morphology is presented for various $Na_x(Ni\text{-}ett)_n$ loadings. Optical transmission microscopy (**Figure 1**a) of relatively thin drop-casted films (typical thickness: 5-8 μm) reveals that a $Na_x(Ni\text{-}ett)_n$ loading higher than 50 wt.% generates inhomogeneous and incoherent films, as a result of an extended agglomeration of $Na_x(Ni\text{-}ett)_n$ particles. Scanning electron microscope (SEM) is used to further investigate the external surface morphology (**Figure 1**b) and cross-sectional areas (insets of **Figure 1**b) of 10, 50 and 70 wt.% NL films. For low $Na_x(Ni\text{-}ett)_n$ contents (e.g. 10 wt.%), a relatively good dispersion can be observed. For loading above 50 wt.%, the agglomeration of $Na_x(Ni\text{-}ett)_n$ particles, appearing as dark dots, is evident. NL films, containing $Na_x(Ni\text{-}ett)_n$ concentration higher than 70 wt.%, present cracks and defects throughout the whole volume of the sample, confirming the inability of $Na_x(Ni\text{-}ett)_n$ to form a coherent matrix. SEM images of the cross sectional areas (insets of **Figure 1**b) show that a porous structure emerges with increasing $Na_x(Ni\text{-}ett)_n$ content. To improve the coherence of NL films at high $Na_x(Ni\text{-}ett)_n$ content, the film thickness (typical thickness: 5 - 8 μm) is increased by depositing multiple drop casted layers. This allows even NL films with more than 70 wt.% of $Na_x(Ni\text{-}ett)_n$ to be peeled off from the glass substrates (**Figure S2**) and tested for their mechanical properties (**Figure 1**e-f).

Typical stress-strain curves of NL films are shown in **Figure 1**e. The strain-at-break monotonically decreases with increasing $Na_x(Ni\text{-}ett)_n$ content (from ~1000% of pure Lycra® films down to (18.0 ± 0.2)% for the 70 wt.% NL film) while the elastic modulus increases (from (6.0 ± 0.9) MPa for pure Lycra® to (23.6 ± 2.3) MPa for the 50 wt.% NL film) (**Figure 1**f). This is the typical behaviour of polymer composites containing rigid brittle particles, described by many micromechanical models. [20] $Na_x(Ni\text{-}ett)_n$ concentrations higher than 50 wt.% results in inhomogeneous, brittle films and a decrease of both elastic modulus and strain-at-break. NL films with a $Na_x(Ni\text{-}ett)_n$ content lower than 50 wt.% can be candidates for stretchable strain sensors, provided that they retain the thermoelectric properties of $Na_x(Ni\text{-}ett)_n$. In the next

section, we show that these films have also good electrical conductivities, Seebeck coefficients and power factors.

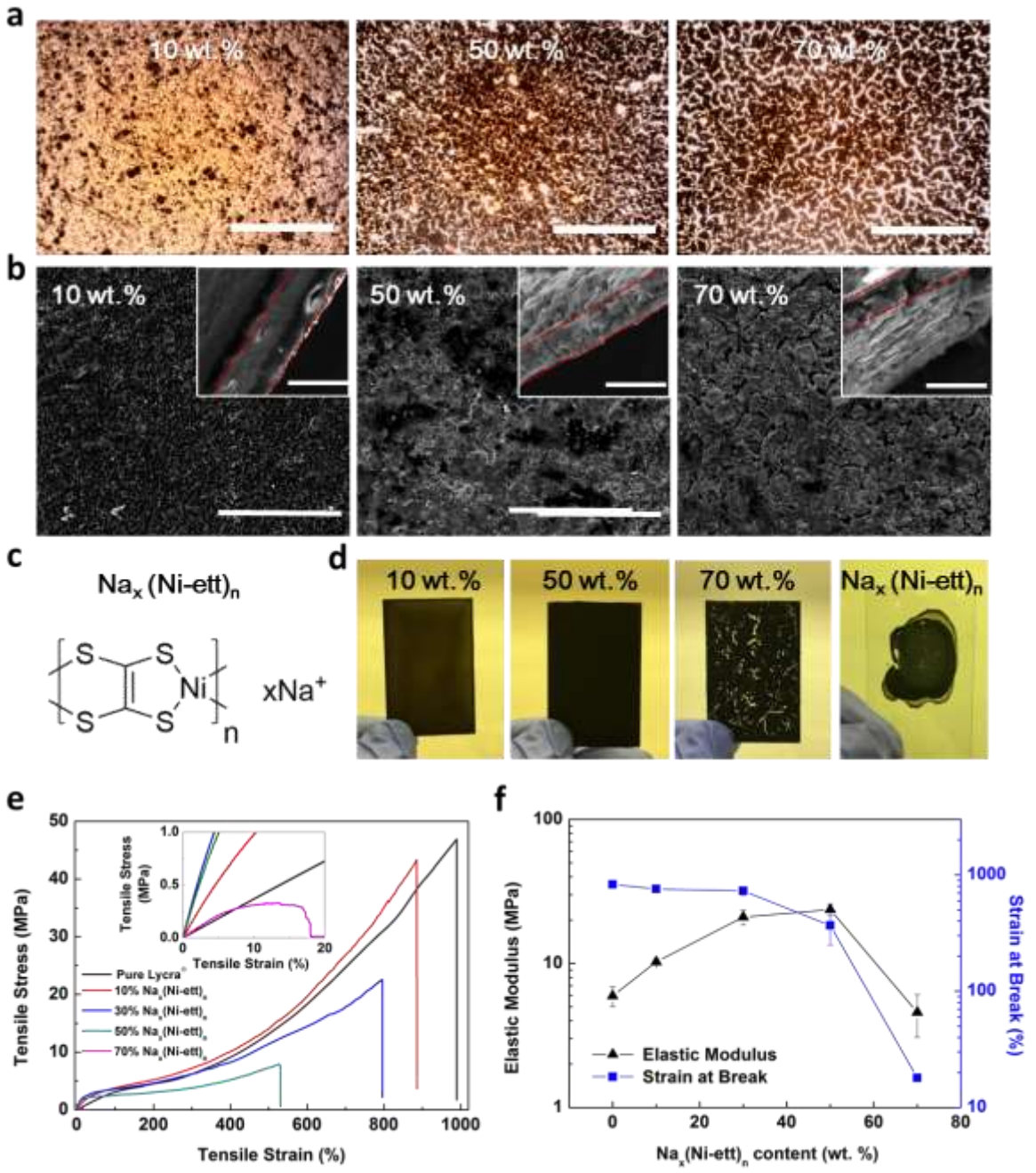

Figure 1. Morphological and mechanical studies of NL films containing different $Na_x(Ni\text{-}ett)_n$ concentrations. (a) Optical microscopy pictures (scale bars are 500 μm), (b) scanning electron microscopy of top surface (scale bars are 100 μm) and cross sections (inset; scale bars are 10 μm) of one layer 10, 50 and 70 wt.% NL films; broken red lines identify the borders of the cross

sections; (c) $Na_x(Ni\text{-}ett)_n$ chemical structure; (d) digital optical pictures of multi-layer NL films on glass slides; (e) typical stress-strain curves and (f) elastic modulus and strain-at-break of self-standing NL films.

2.2. Thermoelectrical properties

In order to evaluate the thermoelectric properties of the NL films and their potential use in self-powered sensors, both Seebeck coefficient (S) and electrical conductivity (σ) have been measured. The corresponding power factor (PF) have been calculated according to: $PF = S^2 \times \sigma$. Conversely to the usual inverse relationship between S and σ, requiring properties' trade-off in traditional inorganic TE materials, **Figure 2a** shows a monotonic trend for S and σ, both increasing with the $Na_x(Ni\text{-}ett)_n$ content. The behavior of σ with the $Na_x(Ni\text{-}ett)_n$ amount is expected from percolation theory [21]: the conductivity increases due to a densifying conductive network until it reaches a plateau determined by the conductivity of $Na_x(Ni\text{-}ett)_n$. The trend of the Seebeck coefficient is less intuitive but not unusual for heterogeneous composite systems.[22] This phenomenon has been explained by enhancement of carrier mobility as the percolated network becomes more robust upon densification. [23]

The PF of the NL composite films reaches 0.9×10^{-3} μW m^{-1} K^{-2} and 1.3×10^{-3} μW m^{-1} K^{-2} for films with $Na_x(Ni\text{-}ett)_n$ concentration of 50 wt. % and 70 wt. %, respectively. An accurate ZT (the dimensionless figure of merit: $ZT = \frac{S^2\times\sigma}{\kappa}\,T$) value cannot be reported as the thermal conductivity (κ) of the films is difficult to measure in the in-plane direction. However, an upper limit of thermal conductivity can be predicted from the values relative to the individual phases: ~ 0.15 W m^{-1} K^{-1} for polyurethane [24] (a polymer similar to Lycra) and ~0.2 W m^{-1} K^{-1} for $Na_x(Ni\text{-}ett)_n$ (at 27 ºC) [16] by a simple series-model and parallel model (**SI Note S1**). The

thermal conductivity of 50 wt. % NL film estimated is ~ 0.17 W m^{-1} K^{-1}. Hence a *ZT* in the region of 3×10^{-7} can be expected. Comparing to the results of the other poly(Ni-ett) materials[16-17, 25], this is relative low, but it is comparable to polymer composites containing poly(Ni-ett) [18a, 26]. The low *PF* value is most ascribe to the low electrical conductivity. But a low electrical conductivity combined with a filler content close to percolation threshold, can be beneficial to gain a highly sensitive resistive sensor.

Due to its high extensibility (strain at break of ~500%) and thermoelectric properties, the 50 wt.% NL composite film is selected to further study its self-powered sensing ability, as presented in the following sections.

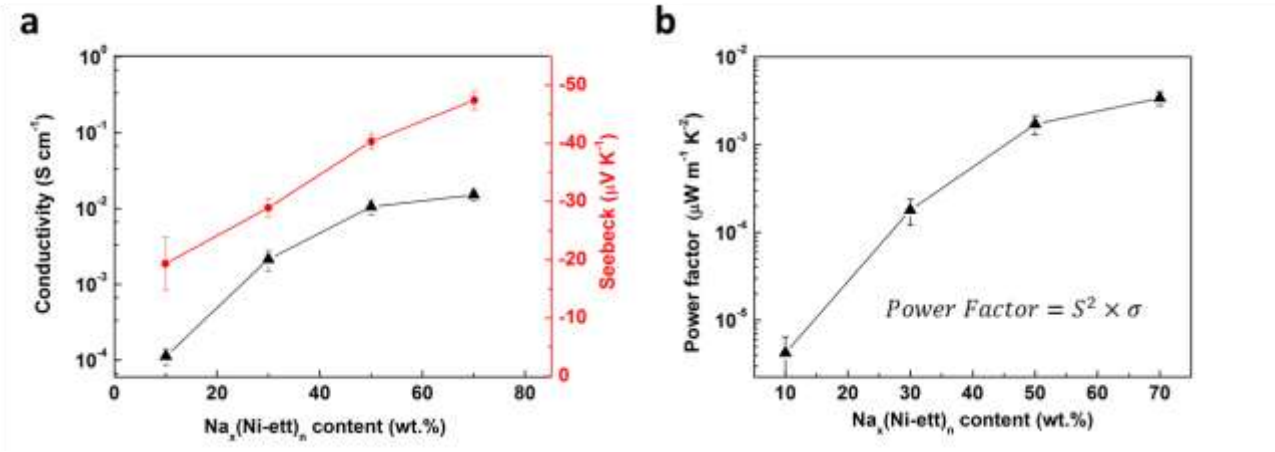

Figure 2. Thermoelectric properties of NL films. (a) Electrical conductivity, Seebeck coefficient and (b) Power factor.

2.3. Self-powered strain sensing

To examine the capabilities of utilising the fabricated NL films as self-powered strain sensors, the electrical resistance and Seebeck voltage have been monitored *in-situ* under different strain stimuli.

In order to evaluate the strain sensitivity of the 50 wt. % NL film, a constant external power has been supplied to its extremities (**Figure 3**c). The electrical resistance has been measured while deforming the film uniaxially, at a constant extension rate, until break. The resistance variation ($\Delta R/R_0$, with $\Delta R = R - R_0$, where R is the electrical resistance at a given extension, and R_0 is the initial resistance) increases linearly with the extension (**Figure 3**a). The strain sensitivity of a sensor is usually represented by its gauge factor, *GF*, defined as $GF = (\Delta R/R_0)/\varepsilon$,[27] where ε is the strain. **Figure 3**a shows the *GF* exceeds 20, in the range of deformations between 5% and 50%, compared with values of ~2 for traditional metal-based strain gauges. [28] Notably, the gauge factor preserves a high value (~ 13) even for strains as high as 300%. To the best of our knowledge this is the highest *GF* value reported for such high strain range.[29]

The change in electrical resistance in our sample upon uniaxial deformation can be caused by two concurrent factors: the dimensional changes of the sample, and the changes in the conductive network (i.e. changes in the composite electrical resistivity). The geometrical contribution, $\frac{\Delta R_g}{R_0} = \varepsilon(2 + \varepsilon)$ [30] (assuming that the volume of the material remains constant), is not sufficient to explain the experimental resistance variation (**Figure 3**d). The percolated network formed by the conductive Na_x(Ni-ett)$_n$ domains must be affected by the uniaxial deformation, i.e., the intrinsic conductivity of the NL films must change with strain.

Aiming to demonstrate the concept of self-powered (strain) sensing based on the TE effect, a constant temperature difference (ΔT ~ 50 ^{o}C) is applied to the 50 wt.% NL film, by fastening a heat pad to one end of the film, via the lower clamp of the tensile testing set-up (**Figure 3b, 3e**). A thermal voltage developed along the film, in proportion to the temperature difference. When the sample is connected in series to a resistor, R_L, a thermal current can also be generated. **Figure 3**f shows that both current and voltage change as a function of the imposed strain (applied in a sequence of different cycles with max strains of 5, 10, 30, 50, 80 and 100%), demonstrating the ability to sense and generate thermoelectric power concurrently. The

simultaneous change in voltage and current with strain (**Figure 3**f) can be explained in terms of the equivalent circuit of **Figure 3**e. The constant temperature difference along the film generates the thermal voltage *(U*), which is assumed to be independent from the strain. However, the increase in sample resistance (R_s) with the strain lowers the thermal current generated: $I(\varepsilon) = \frac{U}{Rs(\varepsilon)+RL}$. Consequently, the voltage measured across the load resistor is smaller ($V(\varepsilon) = I(\varepsilon)RL$), in agreement with the signal of voltage and current shown in **Figure 3**f. Therefore, based on the specific application, either signal could be chosen for sensing.

It should be noted that there is a limit to the maximum temperature difference that can be effectively employed. The lower bound of the cold side temperature is related to the glass transition temperature of Lycra (below -60 ºC) [31]. The hot side temperature is limited by the softening temperature of Lycra (~180 ºC [32]), well before reaching the degradation temperature of $Na_x(Ni\text{-}ett)_n$ (~340 ºC, **Figure S3**). Even at lower temperatures, there might be some non-recoverable deformations and viscoelastic stress relaxation effects, as shown in **Figure 3**f (hot side: 75 ºC). In the specific case of the NL films, the maximum temperature difference can be estimated to about 70 ºC , and the maximum thermovoltage generated of ~ 3 mV (for a single film).

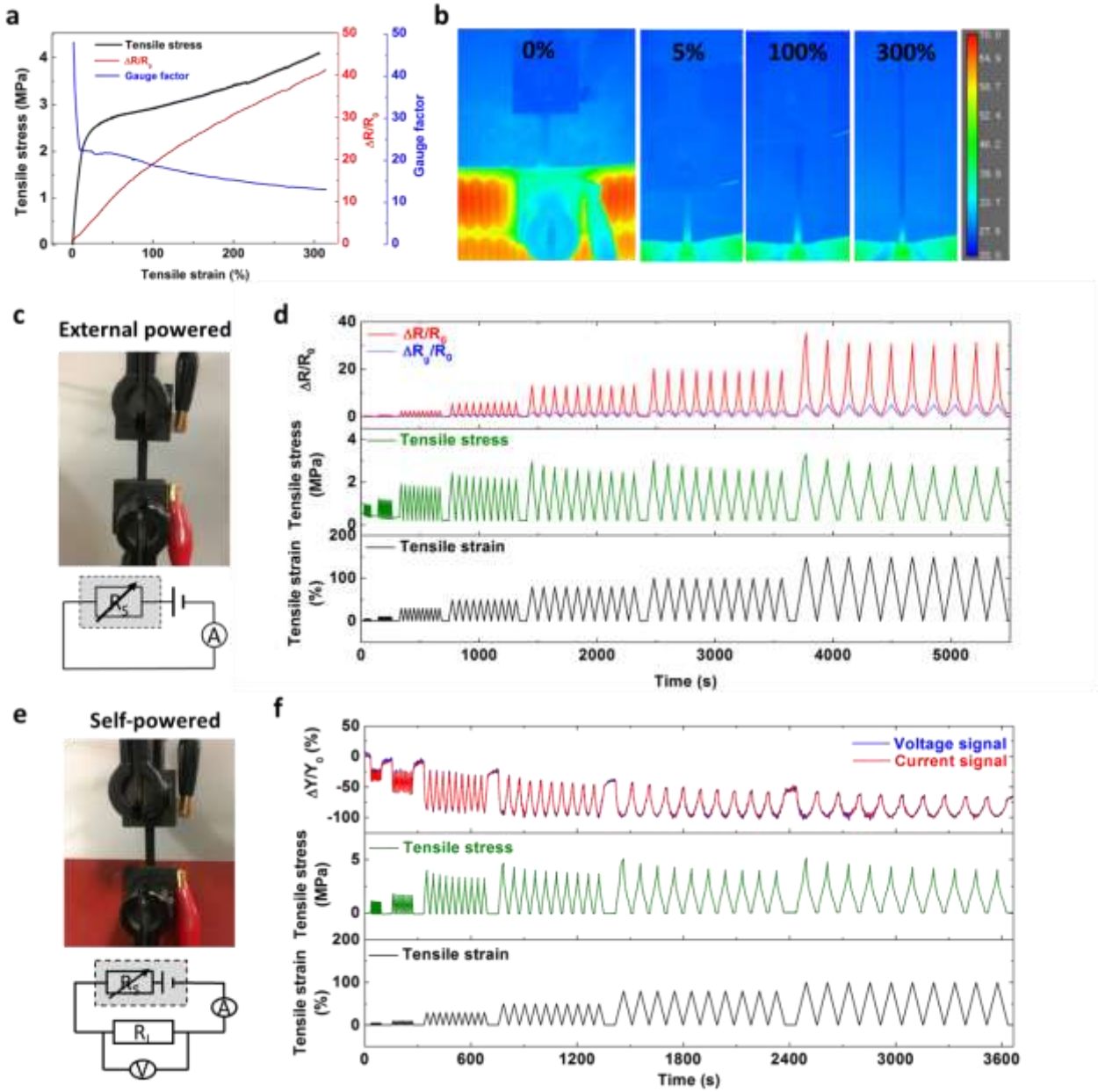

Figure 3. Strain sensing of 50 wt.% NL films. (a) Typical stress-strain curves with its resistance variation ($\Delta R/R_0$) and corresponding gauge factor, as a function of applied strain. (b) Infrared pictures of the temperature difference along the film by contacting one end with a heating pad (T ~ 70 °C), and deformed at different strains. Digital pictures of the set-ups and schematic circuits of (c) the externally powered strain sensor and (e) the self-powered strain sensor. The grey rectangles refer to the equivalent elements of the film during measurements; R_s is the NL film's internal resistance and R_L is the external load. Under cyclic tensile strains applied, (d) actual and geometrical resistance change when worked as externally powered

sensor, and (f) real-time signals change ($\Delta Y/Y_0$ refers to the change percentage of voltage or current) as a self-powered sensor.

2.4. Self-powered visible light sensor

The same NL films can simultaneously sense other stimuli, like visible light. A 50 wt.% NL film was irradiated with visible light fibre source (wavelength ranging from 400 to 900 nm), at different radiation intensities, while maintaining a ΔT_0 ~50 ^{o}C. Considering that the charge carrier density could be affected by the light, it is important to characterise the Seebeck coefficient and the electrical conductivity before and during irradiation. **Figure 4**a demonstrates that the Seebeck coefficient and conductivity do not change significantly with an irradiation intensity of 2 kW m^{-2}, when the surrounding temperature is controlled, which excludes any photo-Seebeck effect or photoelectric effect. In fact, it can be seen that the main effect of light irradiation is in changing the sample temperature (**Figure 4**b). The experimental linear relationship between light irradiation and sample equilibrated temperature can be used to design a visible light sensor. In analogy to the aforementioned strain sensing case, the sensitivity to visible light irradiation is first characterised under external power. As shown in **Figure 4**c, the electrical resistance linearly decreases with light intensity. This is related to the increase in sample temperature and corresponds to the typical semiconductors' response to temperature. Higher temperatures increase the electrons' kinetic energy and the likelihood of electrons to transit from the valance band to the conductive band (**Figure S4**), i.e., thermal excitation of carriers into the conduction band.

For the evaluation of self-powered sensor, the power output value as a function of the temperature (difference) variation has been measured in advance. The sample was irradiated whilst simultaneously applying a temperature difference by the same set-up used in the self-powered strain sensing experiments. In this case, the open-circuit voltage, *U* suddenly decreases

upon irradiation (inset of **Figure 4**d). **Figure 4**d shows a linear correlation between *U* and the irradiation intensity, linked to the Seebeck effect: $U = S\,\Delta T$, where the light irradiation heats the whole film including the cold side, thus the temperature difference (ΔT) between the ends of the film decreases and the generated thermal voltage *U* becomes smaller. We can use the measured open-circuit voltage to calculate the temperature difference across the film ($\Delta T = \frac{U}{S}$) and sample temperature (and irradiation intensity by the linear relationship in **Figure 4**b) by $T = \Delta T_r - \frac{U}{S}$, where the ΔT_r is the referenced constant temperature difference, here is 70 °C. Cyclic tests also have been performed with different light intensities over a time interval of 30 s, followed by 30 s of light off. **Figure 4**f and **Figure S5** show a good reproducibility, stability and reversibility. By the same measurement circuit as in the case of strain sensing, the normalised current and voltage can be recorded. We can define a sensitivity factor (*SF*), analogous to strain gauge-factor, as:

$$SF \equiv \left|\frac{\Delta Y/Y_0}{\Delta X}\right| \qquad \textbf{Equation (1)}$$

where ΔX, ΔY refers to the environment stimuli and NL films response signals, respectively. Y_0 is the initial value of the NL films response signal. Here, the resistance signal to irradiation *SF* is ~ 18% $(\text{kW m}^{-2})^{-1}$ and open circuit voltage *SF* is ~ 36% $(\text{kW m}^{-2})^{-1}$.

It is also worth to underline that it is possible to discriminate the signals caused by light irradiation from those caused by a mechanical strain.[33] By recording the I-V curve of the materials, the I-intercept change refers to the irradiation intensity (temperature difference) change, while the slope changes (*R*) refers to the strain.

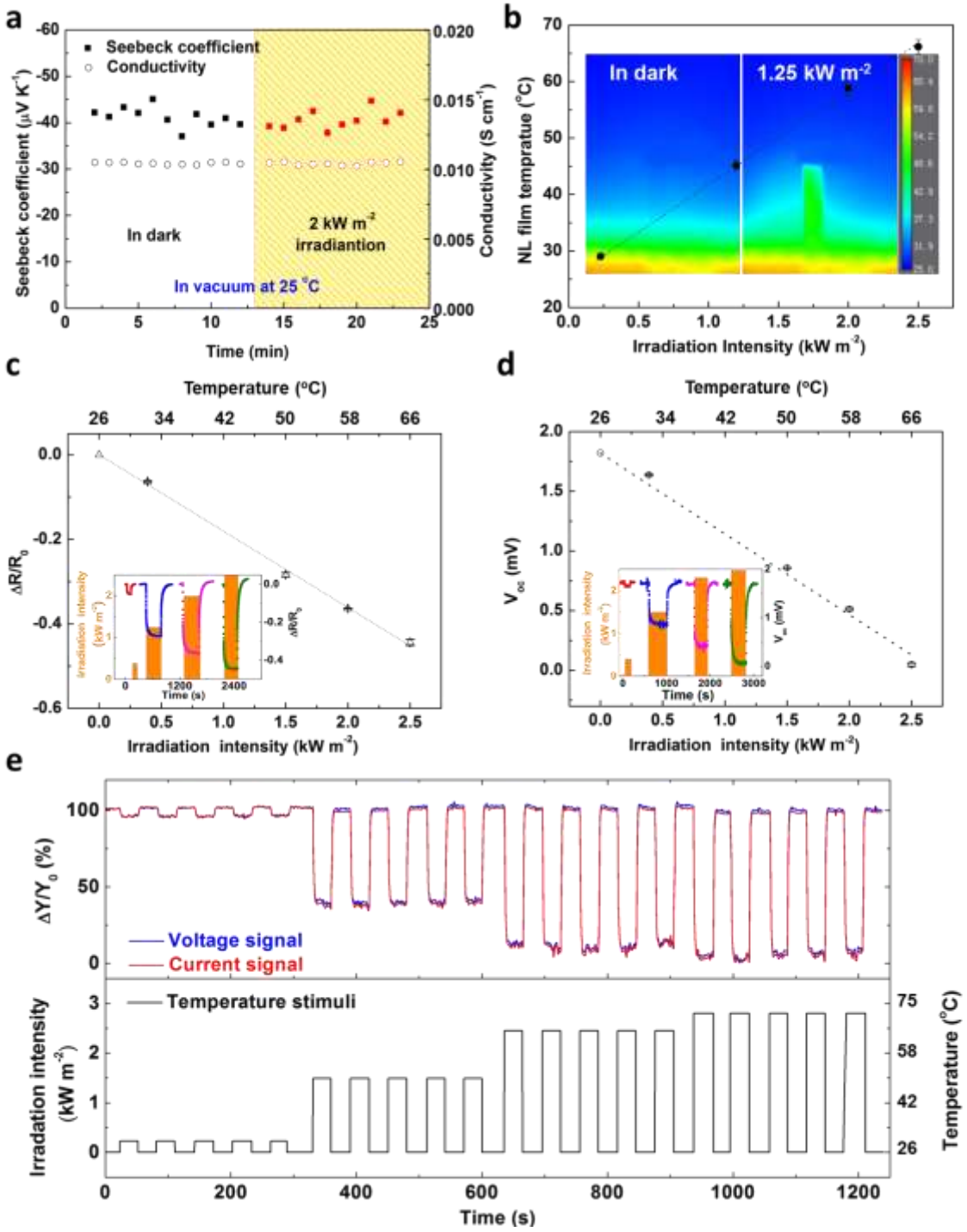

Figure 4. Sensitivity to visible light irradiation of 50 wt.% NL film in the case of externally-powered and self-powered. (a) Seebeck coefficient and electrical conductivity of 50 wt.% NL film, measured in vacuum and under controlled temperature, with/without irradiation. (b) The sample temperature changes with 30 s interval of light at different intensity irradiations, and a representative infrared camera image. (c) Electrical resistance variation and (d) open circuit

voltage (V_{oc}) change with different irradiation intensities, averaged over 5 cyclic tests (representative signal curves of these cyclic tests are shown in the insets). (e) Signals change ($\Delta Y/Y_0$ is change percentage of voltage across or current through the 10 kΩ load resistor), recorded while irradiated cyclically over time.

2.5. Sensitivity to humidity

In an attempt to explore sensitivity to other stimuli and, equally importantly, exclude problems of cross-sensitivities, the effect of relative humidity (RH) on the thermoelectric properties of the 50 wt.% NL film have been studied. The resistance variation of the externally-powered sensor placed in a controlled humidity chamber is barely affected by the humidity, both in the case of a quasi-static (**Figure 5** a,b) and cyclically increasing (**Figure 5** c,d) values of humidity. A decrement lower than 12% can be detected when RH increases from 5% to 90% (**Figure 5**a), which gives a *SF* as small as ~ 0.1 % $(\%RH)^{-1}$ (according to **Equation 1**). This small resistance variation can be explained by the presence of a polar solvent [34] (water), which can reduce the Coulombic interactions between the Na^+ ions in Ni-ett and increase their mobility. This hypothesis is compatible with the very weak ionic behaviour that can be observed in our sample: **Figure 5**b shows the perfect semi-circuits. Although, electrical and ionic conductivity [34] are jointly present in that semicircle, the weak humidity dependence of the resistance (**Figure 5**c) indicates that electronic conductivity is dominant. Under a $\Delta T \sim 25\ ^oC$, the open-circuit voltage *U* is essentially independent from RH (**Figure 5**d), with very small fluctuations induced by air flow.

The simultaneous self-powered sensitivity to strain and temperature and insensitivity to humidity of our NL films might be particularly desirable in certain applications like in smart packaging and wearable technologies.

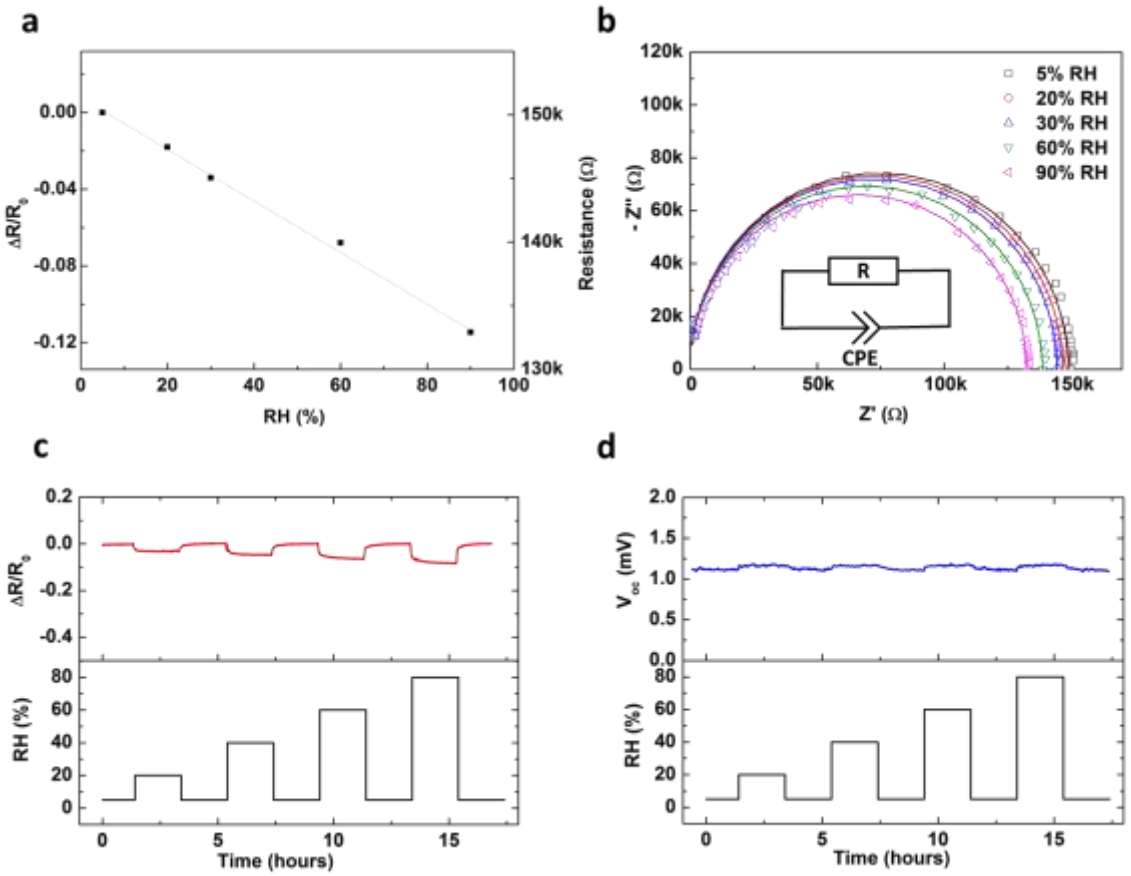

Figure 5. Sensitivity of the 50 wt.% NL film in externally- and self-powered configurations to relative humidity (RH). (a) The AC (fitted results) resistance variation with RH (data collected after 1 hour at the applied RH level to allow the sensor to stabilise). (b) Nyquist plots and equivalent circuit fitting curves of NL film at different humidity. Resistance (R) contributes in parallel to the constant phase element (CPE). (c) Resistance variation ($\Delta R/R_0$) and (d) open-circuit voltage (V_{oc}) response to RH cycles.

2.6. Multi-leg device assembly

The power harvested with a single NL film, for a ΔT of 30 ^{o}C, is of the order of few pW. To satisfy the power demand of an integrated self-powered system, a power output of at least 3 – 100 μW[35] is required. This could be achieved by (i) increasing the temperature difference; (ii) connecting our n-type NL material with a p-type TE counterpart in series to form a p–n junction;

and connecting many p-n junctions in series, (iii) optimise the size and shape of each leg. If the first strategy is constrained by the maximum temperature range, as discussed before (**Section 2.3**), the latter two are more flexible and viable to increase power output. Our group has recently developed a p-type organic TE compound, based on blends of Lycra® and PEDOT:PSS[15], which is an ideal candidate for a (multi-leg) all-organic stretchable TE device.

In deciding how to best connect p- and n-type legs instead of the in-plane connection (**Figure S6**f), one could look at the current state-of-the-art. As schematically illustrated in **Figure 6**a, series of p-n junctions have simply been created by hot pressing at 160 °C the p-type (Lycra®/PEDOT:PSS [15]) and n-type (Lycra®/Na_x(Ni-ett)$_n$) legs with an interposed flexible electrical insulation layer (polyurethane film). This process is potentially continuous, fast and scalable, which is critical for any future large scale industrial adoption. The junction between p- and n-type legs created by hot pressing is robust (see SEM micrographs of the cross-sectional area in **Figure 6**a), and the TE device remains flexible (**Figure S6**) even in the case of a relatively large thickness.

The power outputs of different TE devices, with an increasing number of p-n junctions, have been measured for different external load resistances (**Figure 6**b,c). As expected, both the open-circuit voltage U and the maximum power output P_{max} increase with the number (n) of p-n junctions (**Figure 6**b), in accordance with the following equations:

$$\mathrm{U} = n(\alpha_p + \alpha_n)\Delta T \qquad \textbf{Equation (2)}$$

$$P_{max} = \frac{U^2}{2(n(R_p+R_n)+(2n-1)R_{p-n})} \qquad \textbf{Equation (3)}$$

where α_p, R_p, α_n and R_n are respectively the absolute values of Seebeck coefficient and resistance of the p and n legs. $R_{p\text{-}n}$ refers to the contact resistance between p-type and n-type materials which could hinder carrier transport. These equations show that $U \propto \Delta T$ and when

$R_{p\text{-}n}$ is much smaller than $R_p + R_n$, it can been simplified into $P_{max} \propto \Delta T^2$, which is in agreement with experimental data of **Figure 6**c. Meanwhile, based on the film low thermal conductivity, it is suitable to increase the cross section area and decrease length in order to decrease the resistance (R_L). **Figure 6**d,f shows, on a single n-type leg, how this kind of geometric optimisation can boost power output by at least an order of magnitude.

Extrapolating these results and using **Equation 2** and **3**, it can be estimated that 55.6 k couples, with dimensions of 1 mm × 3 mm× 3 mm (calculation as **SI Note S2**), are required to reach a power output of 10 μW, for a ΔT of 10 ºC. The main limitation is the poor conductivity, but recent reports have presented improvements in both conductivity and Seebeck. Taking the best conductivity results (50 S cm^{-1}) of $Na_x(Ni\text{-}ett)_n$ with insulating composites as example, only 22 couples would be needed. The total device would only be 0.4 cm^3 in volume, provided by the separator is 0.01mm thickness.

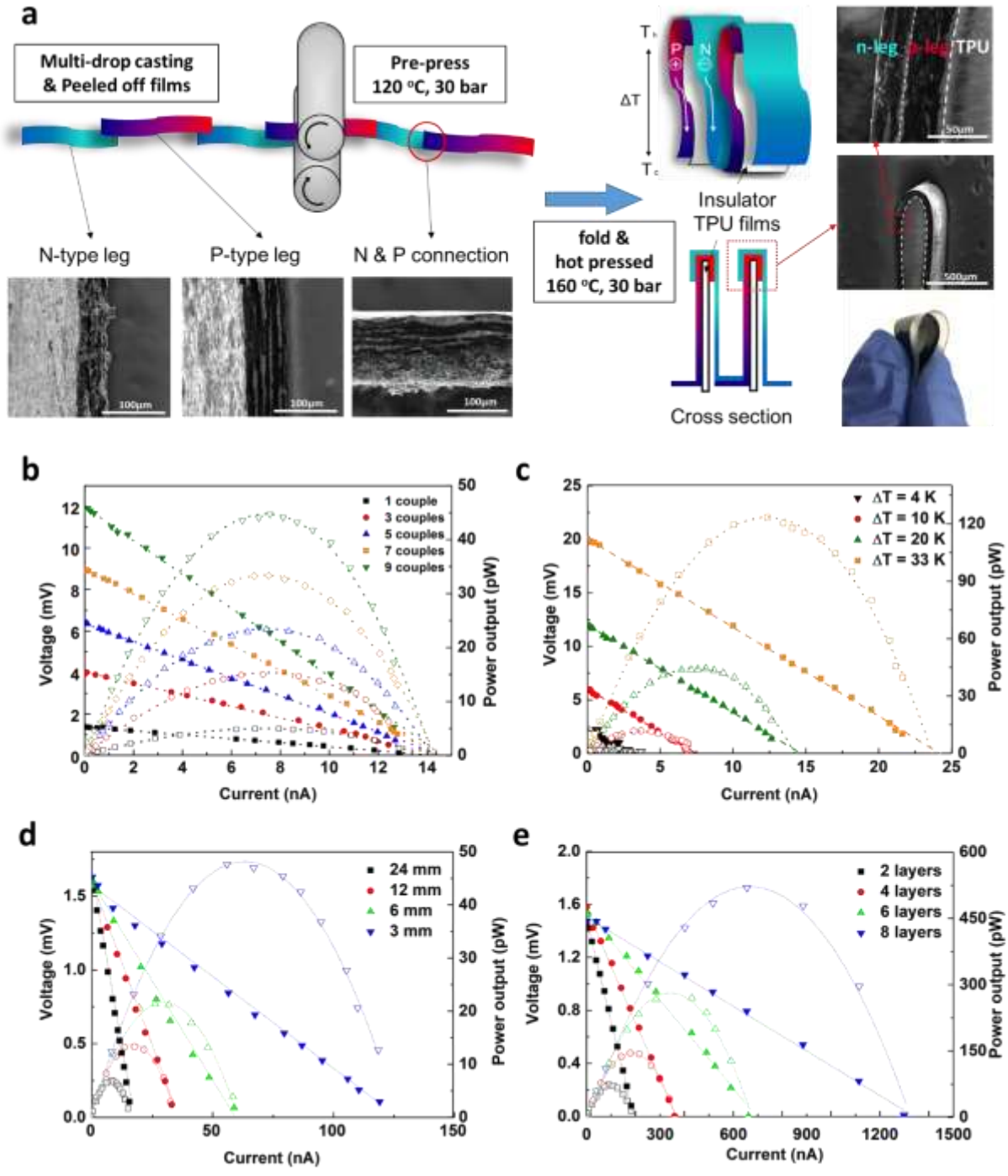

Figure 6. Fabrication and characterisation of organic TE devices based on p-n junctions. (a) Illustrative sketch of the continuous assembly line, with cross-sections of p, n-legs, connections (with Na elements analysis shown as blue dots), a p-n junction, and a digital picture of a folded 1-couple TE device. Open-circuit voltage and power output generated by (b) *n*-couples TE devices at $\Delta T \sim 25$ °C and by (c) a 9-couples TE device at the multi-leg TE device fabrication together with SEM pictures (bottom different temperature differences.

Open-circuit voltage and power output generated by single NL film with (d) different length and (e) thickness (stacking layers of 20 mm length NL films) at $\Delta T \sim 27$ °C. Empty and full symbols in (c-e) indicate power and voltage, respectively.

In order to demonstrate the application of these materials as wearable sensors, an 8-couples TE 'bracelet' device has been used to power a single NL stripe sensor, connected to the index finger, to detect its movements (**Figure 7**a). The electrical connections and signal acquisition system are represented by the equivalent circuit of **Figure 7**a. When the index finger bends to different angles, both current and voltage show clear signal changes (**Figure 7**b). This shows the potential of these materials as self-powered sensors.

Examples of more complicated device architectures have been attempted. For instance an origami-inspired "magic ball".[36] Origami, the ancient art of paper folding, is used here as a method to transform 2D in-plane structures to 3D out-of-plane shapes, constituted by p-n TE legs, connected in series or in parallel in order to increasing power output and reliability. A simple 6-couples TE device (**Figure 7**c) has been fabricated by coating $Na_x(Ni\text{-}ett)_n$ and PEDOT:PSS on a paper as the n and p leg respectively. The power output reaches 30 pW when a temperature difference of 20 °C is applied. Larger TE devices can be fabricated by the same way. Following the design in **Figure S7**, a 90-couples TE device can simply be manufactured (**Figure 7d**), showing the ability to adapt to different shapes, geometries and applications. Among these, one could envisage exploitations as inflating and 3D conformable surfaces, for instance in soft robotic, smart packaging, wearable, automotive and Internet-of-Things.

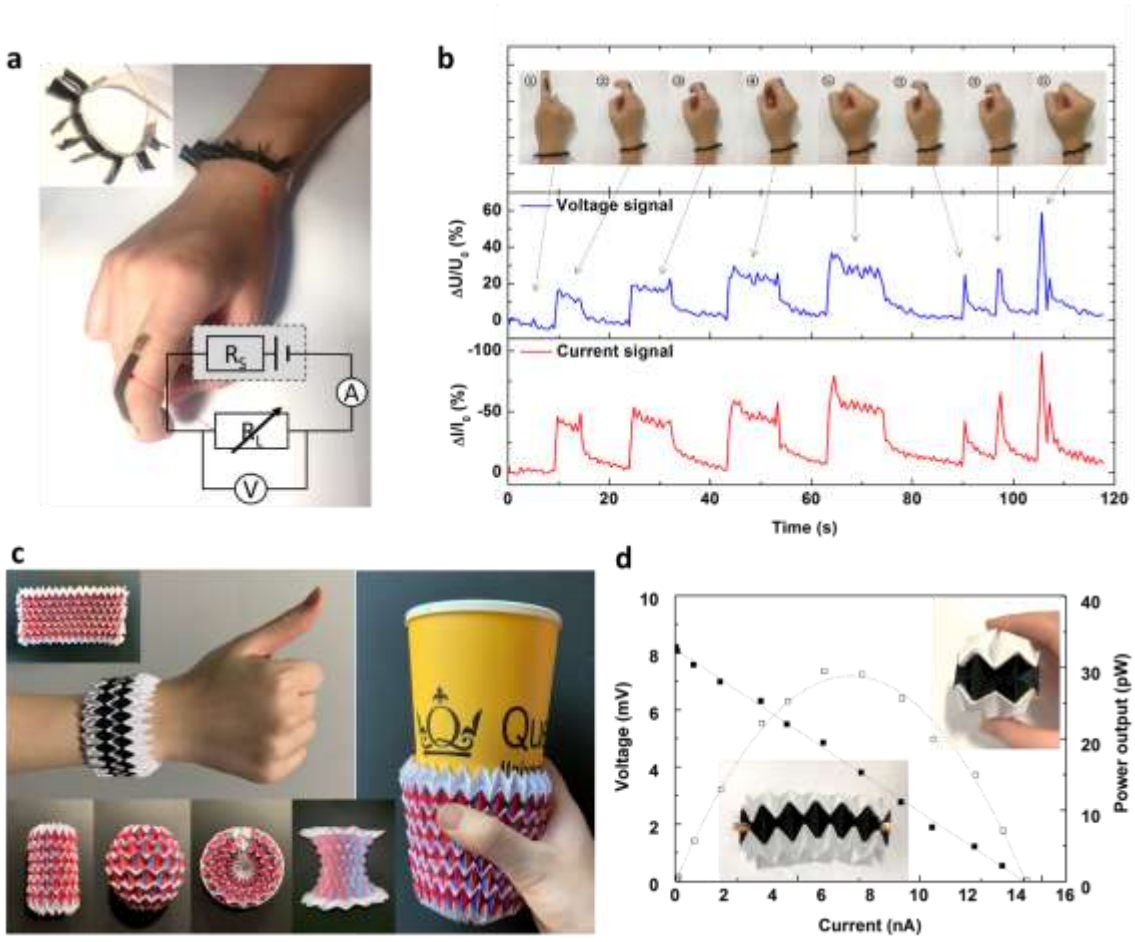

Figure 7. Examples of applications and proof-of-concepts of flexible TE sensing devices. (a) Digital optical pictures, demonstrating a self-powered 'bracelet' TE device. The 'bracelet' is made by the 8-couples and powers a strain sensing NL stripe, working as an index finger motion detector. (b) The response to different positions of the index finger, self-powered by a ΔT of ~ 20 ^{o}C. (c) The multi-couples TE devices, inspired by the origami "magic ball". (d) The power output of 6-couples TE device under ΔT ~ 20 ^{o}C.

3. Conclusion

This work demonstrates a facile strategy to develop stretchable and multifunctional self-powered sensors based on the thermoelectric effect in organic conductors. Greatly improved mechanical properties have been achieved by compounding brittle n-type $Na_x(Ni\text{-}ett)_n$ within a flexible Lycra® matrix, while preserving the thermoelectric properties. For an optimised ratio, with 50 wt % $Na_x(Ni\text{-}ett)_n$, an outstanding strain-at-break of 217 ± 37 % is achieved, in conjunction with the Seebeck coefficient of -40 μV K^{-1} and electrical conductivity of 0.01 S cm^{-1}.

This novel compound has shown sensitivity to different stimuli, like strain and light irradiation. When exposed even to 10-20 ºC temperature difference, the device is also able to generate enough power to enable autonomous sensing.

By exploiting the enhanced processability of our polymer TE compounds, a new manufacturing strategy has been proposed to overcome the typical shortfalls of π-shaped TE devices: brittleness and long and hardly scalable manufacturing processes. Series of p-n junctions could simply be created by hot pressing an n-type leg (Lycra®/$Na_x(Ni\text{-}ett)_n$) with a previously developed p-type leg (Lycra®/PEDOT:PSS), and an interposed flexible electrical insulation layer, with a process which is potentially continuous, fast and scalable. The concept of the self-powered sensor is demonstrated in the detection of an index finger motion. Projecting into the future, an origami inspired inflatable and 3D conformable "magic ball" TE device has also been demonstrated, which might be exploited for instance in soft robotic, smart packaging, wearable electronics, and Internet-of-Things.

4. Experimental section

Preparation of NL films: $Na_x(Ni\text{-}ett)_n$ was synthesized following a reported procedure (also see in **SI Note S3**).[19] And 5 wt·% $Na_x(Ni\text{-}ett)_n$ was dispersed in anhydrous DMSO (> 99.9 %, Sigma Aldrich) by bath sonication (ultrasonic cleaner, VWR) for 30 minutes and stirring for 2 hours, sequentially. It was mixed with 1 wt.·% PU (Lycra® Invista)/DMSO dispersion with different ratios. The content of $Na_x(Ni\text{-}ett)_n$ in final composites film were 10 wt.%, 30 wt.%, 50 wt.%, and 70 wt.%. They were prepared by drop casting approximately 2 ml the mixture on pre-cleaned glass sides (75 mm × 25mm), dried at 80 ℃ in oven under ambient atmosphere. Different casting temperatures were trialled, ranging from 40 ℃ to 140 ℃, shown as **Figure S8**. Repeat 5-8 times drop-casting procedure until the weight of solid was approximately 0.1 g. Self-standing NL films of approximately 50 μm thickness were obtained after drying at 80 ℃ in a vacuum oven for 12 hours and peeling off (as **Figure S2** shown). Cut by a D882-02 standard die, 40 mm × 5 mm NL films were ready for following utilizations.

Fabrication and assembly of multi-leg devices: PEDOT:PSS/Lycra® (PL) films were prepared following a reported procedure.[15] 1 wt·% solids content PEDOT:PSS (Clevios PH1000, Heraeus GmbH) DMSO dispersion was mixed with 1 wt·% Lycra®/DMSO dispersion with proportion of 1:9. Afterwards, the same drop-casting method and drying procedures are used, obtaining the similar thickness and dimension as the NL counterpart.

For the stretchable TE device, PL and NL films were used as p-type and n-type legs, respectively. P&n legs were connected by pre-pressing at 120 ºC, 30 bar for 1 minutes. After folding the continuous legs along the out-of-plane direction and separated by insulating polyurethane films, the device was pressed at 30 bar, 160 ℃ for 5 minutes within a mould. An 8-couple device was used for wearable self-powered sensor demonstration under temperature difference of 20 ºC.

Magic ball shaped generator was fabricated by patterned painting $Na_x(Ni\text{-}ett)_n$ and PEDOT:PSS on a paper as n and p leg respectively, while drying on a 100 ^oC hot plate. Then fold it and connect electrodes as **Figure S7** shows.

Characterisations: Mechanical tests were performed by using a quasi-static tensile tester (Instron 5566) with a rate of 100% min^{-1} following the ASTM D882-02 standard. The Seebeck coefficient was measured at 27 ^oC under nitrogen atmosphere, using the MMR Technology Seebeck Effect Measurement System. A bespoke four-point probe (0.25 mm probe space) made of an Agilent 6614 System DC power supply with Keithley 6485 picoammeter an Keithley 2000 multimeter were used for electrical conductivity measurements. Thickness of films were measured by a Bruker Dektak Vision 64 profilometer. The thermal stability was characterized through thermogravimetric analysis (TA Instruments Q500 Thermogravimetric Analyzer), as shown in **Figure S3**. Scanning electron microscope (SEM) was taken by the FEI Inspect F with an energy dispersive x-ray spectrometry (EDX). Optical microscopy images were obtained by VWR® VisiScope® 384. UV-vis spectra of different ratios of the NL solutions were obtained by Perkin Elmer Lambda35. DMSO as background spectrum was eliminated from the samples spectrums. Photo-Seebeck coefficient was measured by MMR system with surrounding temperature controlled at 27 ^oC and light irradiate through a transparent window. Impedance spectra were measured by using an Autolab Frequency Response Analyser FRA2 with a potentiostat PGSTAT10 (Windsor Scientific, UK), and operated under an AC amplitude of 100 mV peak to peak, DC off-set potential 0 V, and 10 Hz to 10 MHz frequency range.

For external sensor demonstration, a constant voltage (~ 0.5 V) was applied by Agilent 6614 System DC power supply and the current was recorded with the Agilent 34401A 6 ½ digital multi-meter. For self-powered sensor demonstration, heater mats (RS, 12 V dc, 7.5 W, item 245-556 and RS, 12 V dc, 1.25 W, item 245-499) was applied on one side of the NL film, and the other end at room temperature to obtain a constant temperature difference at extremities. A

load resistor (100MΩ) and a picoammeter (Keithley 6485) was connected to NL film in series, and a voltmeter (Keithley 2000 Multimeter) was connected to the load resistor in parallel.

Fibre optic light source (Coherent, model 1-150) was used for visible light sensitivity tests, with irradiation intensity measured by a monocrystalline silicon reference cell (SRC-1000-TC-QZ, VLSI Standards, Inc.). A bespoken humidity controller was set up for humidity tests. 0.6 L min^{-1} different moist nitrogen gas was flow into a ~700 cm^3 chamber which takes ~ 600 s for stabilization. A humidity sensor (Fisher brand) was used for calibration (as shown in **Figure S9)**. Due to the chamber size,

The open circuit voltage and maximum power output were measured by connecting the ends of the fabricated generator with a variable resistor (range from 9 Ω to 999 MΩ) with measuring voltage and current simultaneously.

Acknowledgements

Kening Wan is grateful to the China Scholarship Council for the scholarship supporting, the Leverhulme Trust (RF-2017-655) and European Thermodynamics Ltd. for helpful discussions.

Reference

[1] a) O. Han, T. Jingjing, S. Guanglong, Z. Yang, L. Zhuo, L. Hu, Z. Luming, S. Bojing, F. Yubo, F. Yifan, W. Z. Lin, L. Zhou, *Advanced Materials* **2017**, 29, 1703456; b) W. Gao, S. Emaminejad, H. Y. Y. Nyein, S. Challa, K. Chen, A. Peck, H. M. Fahad, H. Ota, H. Shiraki, D. Kiriya, *Nature* **2016**, 529, 509; c) M. Mimee, P. Nadeau, A. Hayward, S. Carim, S. Flanagan, L. Jerger, J. Collins, S. McDonnell, R. Swartwout, R. J. Citorik, V. Bulović, R. Langer, G. Traverso, A. P. Chandrakasan, T. K. Lu, *Science* **2018**, 360, 915; d) C. M. Boutry, Y. Kaizawa, B. C. Schroeder, A. Chortos, A. Legrand, Z. Wang, J. Chang, P. Fox, Z. Bao, *Nature Electronics* **2018**, 1, 314.

[2] a) M. Wehner, R. L. Truby, D. J. Fitzgerald, B. Mosadegh, G. M. Whitesides, J. A. Lewis, R. J. Wood, *Nature* **2016**, 536, 451; b) S.-J. Park, M. Gazzola, K. S. Park, S. Park, V. Di Santo, E. L. Blevins, J. U. Lind, P. H. Campbell, S. Dauth, A. K. Capulli, F. S. Pasqualini, S. Ahn, A. Cho, H. Yuan, B. M. Maoz, R. Vijaykumar, J.-W. Choi, K. Deisseroth, G. V. Lauder, L. Mahadevan, K. K. Parker, *Science* **2016**, 353, 158.

[3] a) S. Wang, J. Xu, W. Wang, G.-J. N. Wang, R. Rastak, F. Molina-Lopez, J. W. Chung, S. Niu, V. R. Feig, J. Lopez, T. Lei, S.-K. Kwon, Y. Kim, A. M. Foudeh, A. Ehrlich, A. Gasperini, Y. Yun, B. Murmann, J. B. H. Tok, Z. Bao, *Nature* **2018**, 555, 83; b) M. Chunhong, S. Yuanqiang, H. Wutong, R. Ao, S. Rujie, X. Weihua, Z. Huaiwu, *Advanced Functional Materials* **2018**, 28, 1707503; c) Q. Hua, J. Sun, H. Liu, R. Bao, R. Yu, J. Zhai, C. Pan, Z. L. Wang, *Nature Communications* **2018**, 9, 244; d) C. Larson, B. Peele, S. Li, S. Robinson, M. Totaro, L. Beccai, B. Mazzolai, R. Shepherd, *Science* **2016**, 351, 1071; e) Z. Ma, *Science* **2011**, 333, 830.

[4] J. Wang, W. Ding, L. Pan, C. Wu, H. Yu, L. Yang, R. Liao, Z. L. Wang, *ACS Nano* **2018**, 12, 3954.

[5] L. Ju‐Hyuck, L. K. Young, G. M. Kumar, K. T. Yun, L. Dae‐Yeong, O. Junho, R. Changkook, Y. W. Jong, K. Chong‐Yun, Y. Seok‐Jin, Y. Ji‐Beom, K. Sang‐Woo, *Advanced Materials* **2014**, 26, 765.

[6] H. Xue, Q. Yang, D. Wang, W. Luo, W. Wang, M. Lin, D. Liang, Q. Luo, *Nano Energy* **2017**, 38, 147.

[7] S. Daozhi, X. Ming, Z. Guisheng, L. Lei, D. W. W., Z. Y. Norman, *Advanced Materials* **2018**, 30, 1705925.

[8] a) A. K. Menon, O. Meek, A. J. Eng, S. K. Yee, *Journal of Applied Polymer Science* **2017**, 134; b) Y. Xie, T.-M. Chou, W. Yang, M. He, Y. Zhao, N. Li, Z.-H. Lin, *Semiconductor Science and Technology* **2017**, 32, 044003; c) Y.-T. Jao, Y.-C. Li, Y. Xie, Z.-H. Lin, *ECS Journal of Solid State Science and Technology* **2017**, 6, N3055.

[9] C. B. Vining, *Nat. Mater.* **2009**, 8, 83.

[10] a) D. Kraemer, L. Hu, A. Muto, X. Chen, G. Chen, M. Chiesa, *Applied Physics Letters* **2008**, 92, 243503; b) N. Wang, L. Han, H. He, N.-H. Park, K. Koumoto, *Energy & Environmental Science* **2011**, 4, 3676.

[11] D. Zhao, H. Wang, Z. U. Khan, J. C. Chen, R. Gabrielsson, M. P. Jonsson, M. Berggren, X. Crispin, *Energy Environ. Sci.* **2016**, 9, 1450.

[12] D. Zhao, S. Fabiano, M. Berggren, X. Crispin, *Nat Commun* **2017**, 8, 14214.

[13] F. Zhang, Y. Zang, D. Huang, C.-a. Di, D. Zhu, *Nature communications* **2015**, 6, 8356.

[14] P. Slobodian, P. Riha, R. Olejnik, R. Benlikaya, *Carbon* **2016**, 110, 257.

[15] P. J. Taroni, G. Santagiuliana, K. Wan, P. Calado, M. Qiu, H. Zhang, N. M. Pugno, M. Palma, N. Stingelin-Stutzman, M. Heeney, O. Fenwick, M. Baxendale, E. Bilotti, *Advanced Functional Materials* **2018**, 28, 1704285.

[16] Y. Sun, P. Sheng, C. Di, F. Jiao, W. Xu, D. Qiu, D. Zhu, *Advanced Materials* **2012**, 24, 932.

[17] Y. Sun, L. Qiu, L. Tang, H. Geng, H. Wang, F. Zhang, D. Huang, W. Xu, P. Yue, Y.-s. Guan, F. Jiao, Y. Sun, D. Tang, C.-a. Di, Y. Yi, D. Zhu, *Advanced Materials* **2016**, 28, 3351.

[18] a) F. Jiao, C.-a. Di, Y. Sun, P. Sheng, W. Xu, D. Zhu, *Philosophical Transactions of the Royal Society A: Mathematical, Physical and Engineering Sciences* **2014**, 372, 20130008; b) M. Sumino, K. Harada, M. Ikeda, S. Tanaka, K. Miyazaki, C. Adachi, *Applied Physics Letters* **2011**,

99, 093308; c) R. R. Søndergaard, M. Hösel, N. Espinosa, M. Jørgensen, F. C. Krebs, *Energy Science & Engineering* **2013**, 1, 81.
[19] A. K. Menon, E. Uzunlar, R. M. Wolfe, J. R. Reynolds, S. R. Marder, S. K. Yee, *Journal of Applied Polymer Science* **2017**, 134.
[20] R. K. Gupta, E. Kennel, K.-J. Kim, *Polymer nanocomposites handbook*, CRC press, **2009**.
[21] D. Stauffer, A. Aharony, *Introduction to percolation theory: revised second edition*, CRC press, **2014**.
[22] a) W. Fan, C.-Y. Guo, G. Chen, *Journal of Materials Chemistry A* **2018**, 6, 12275; b) N. Toshima, *Synthetic Metals* **2017**, 225, 3.
[23] I. Petsagkourakis, E. Pavlopoulou, E. Cloutet, Y. F. Chen, X. Liu, M. Fahlman, M. Berggren, X. Crispin, S. Dilhaire, G. Fleury, G. Hadziioannou, *Organic Electronics* **2018**, 52, 335.
[24] Z. Han, A. Fina, *Progress in Polymer Science* **2011**, 36, 914.
[25] Y. Sun, J. Zhang, L. Liu, Y. Qin, Y. Sun, W. Xu, D. Zhu, *Science China Chemistry* **2016**, 59, 1323.
[26] a) A. K. Menon, R. M. W. Wolfe, S. R. Marder, J. R. Reynolds, S. K. Yee, *Advanced Functional Materials* **2018**, 28, 1801620; b) R. M. W. Wolfe, A. K. Menon, T. R. Fletcher, S. R. Marder, J. R. Reynolds, S. K. Yee, *Advanced Functional Materials* **2018**, 28, 1803275.
[27] C. Pang, G.-Y. Lee, T.-i. Kim, S. M. Kim, H. N. Kim, S.-H. Ahn, K.-Y. Suh, *Nature materials* **2012**, 11, 795.
[28] A. L. Window, *Strain gauge technology*, Springer, **1992**.
[29] a) M. Amjadi, Y. J. Yoon, I. Park, *Nanotechnology* **2015**, 26, 375501; b) S. Gong, D. T. H. Lai, B. Su, K. J. Si, Z. Ma, L. W. Yap, P. Guo, W. Cheng, *Advanced Electronic Materials* **2015**, 1, 1400063.
[30] C. S. Boland, U. Khan, C. Backes, A. O'Neill, J. McCauley, S. Duane, R. Shanker, Y. Liu, I. Jurewicz, A. B. Dalton, J. N. Coleman, *ACS Nano* **2014**, 8, 8819.
[31] A. H. Fawcett, T. M. McNally, *Journal of Applied Polymer Science* **2000**, 77, 586.
[32] G. Bhat, S. Chand, S. Yakopson, *Thermochimica Acta* **2001**, 367-368, 161.
[33] S. Han, F. Jiao, Z. U. Khan, J. Edberg, S. Fabiano, X. Crispin, *Advanced Functional Materials* **2017**, 27, 1703549.
[34] H. Wang, U. Ail, R. Gabrielsson, M. Berggren, X. Crispin, *Advanced Energy Materials* **2015**, 5.
[35] a) Z. Zou, Q. Chen, I. Uysal, L. Zheng, *Philosophical Transactions of the Royal Society A: Mathematical, Physical and Engineering Sciences* **2014**, 372, 20130313; b) X. Liu, E. Sánchez-Sinencio, *IEEE Journal of Solid-State Circuits* **2015**, 50, 1424; c) X. Zhang, Z. Zhang, Y. Li, C. Liu, Y. X. Guo, Y. Lian, presented at 2015 IEEE Asian Solid-State Circuits Conference (A-SSCC) **2015**.
[36] a) D. Lee, J. Kim, J. Park, S. Kim, K. Cho, presented at 2014 IEEE International Conference on Robotics and Automation (ICRA), 31 May-7 June 2014, **2014**; b) Y. Chen, H. Feng, J. Ma, R. Peng, Z. You, *Proceedings of the Royal Society A: Mathematical, Physical and Engineering Sciences* **2016**, 472, 20150846; c) P. H. Le, Z. Wang, S. Hirai, presented at 2015 IEEE International Conference on Advanced Intelligent Mechatronics (AIM), 7-11 July 2015, **2015**.